ChemComm

ROYAL SOCIETY OF CHEMISTRY

COMMUNICATION

View Article Online
View Journal | View Issue

Check for updates

Cite this: *Chem. Commun.*, 2023, **59**, 1845

Received 30th October 2022,
Accepted 17th January 2023

DOI: 10.1039/d2cc05888j

rsc.li/chemcomm

Defect engineering of molybdenum disulfide nanosheets boosting super Zn^{2+} storage from polyaniline intercalation†

Rui Sun, Siyang Dong, Jiekai Yang, Jing Xiong, Caihong Wang, Shengjun Lu,*
Yufei Zhang* and Haosen Fan *

In this work, peony-like structured MoS_2 with intercalation of polyaniline and crystal defects was prepared by a simple hydrothermal method. The defect-rich structure and broad interlayer distance can effectively provide vast ion transport paths to enhance the ion diffusion rate. PA-MoS_2 can maintain 157.7 mA h g^{-1} at 0.1 A g^{-1} after 80 cycles and 77.8 mA h g^{-1} at 1 A g^{-1} after 750 cycles.

Lithium-ion batteries (LIBs) play a vital role in the field of secondary batteries owing to their high specific capacity as well as power density.[1] Other secondary batteries, including sodium-ion,[2–4] potassium-ion,[5,6] and zinc-ion batteries[7,8] are exploited as potential alternatives for LIBs in energy storage. Among of them, aqueous zinc-ion batteries (ZIBs) have successfully attracted great research attention due to their outstanding theoretical specific capacity (820 mA h g^{-1}) and negative potential. However, their reversible capacity has been hindered and impeded by the electrostatic repulsion of zinc ions and low potential windows. Therefore, it is urgent to seek suitable cathode materials to improve Zn^{2+} storage property.[9] Up to now, Mn-based, V-based and Prussian blue analogs (PBA) materials have been widely used as cathodes for ZIBs. Mn-based electrode shows high voltage windows and distinguished rate properties. However, the dissolving of Mn^{2+} in electrolyte during the (dis)charge process extremely bars the long-cycle performance.[10,11] Though V-based materials own super long-cyclic stability and excellent reversible capacity, whether the vanadium pentoxide or vanadate, both of them will bring a negative impact on the environment.[12,13] Besides, PBA embraces a superior voltage plate (1.5 V) than that of V-based cathodes (0.8 V). Unfortunately, it delivers a poor reversible capacity of 50–80 mA h g^{-1} and inferior cycling stability.[14,15] Fortunately, the layered transition metal sulfides have been presented as promising cathodes for ZIBs. Their large layer spacing can accelerate the transport of charge and release the volume variation during the (de)intercalation periods.[16–18] MoS2 is a layered metal sulfide with weak der Waals forces and low energy for insertion metal cations.[19,20]

In this work, peony-like structural 2H-MoS_2 nanosheets with the intercalation of polyaniline serve as a cathode of AZIBs. The polyaniline (PA) was successfully intercalated into the interlayer space of the material, and not only acts as a "pillaring" to support the structural stability but also enlarges the lattice spacing to provide abundant Zn^{2+} diffusion transport channels. A schematic illustration of the intercalation/extraction process of Zn-ions during the cycling process is shown in Fig. S1 (ESI†). The MoO_3 nanobelt (Fig. S2a and b–d, ESI†) was prepared as a precursor for synthesizing MoS_2 and PA-MoS_2. After the hydrothermal sulfidation process, the MoS_2 was successfully prepared (Fig. S3a, ESI†). Interestingly, because of the long-term high temperature sulfidation process, the nanobelt structure of MoO_3 was destroyed. The MoS_2 demonstrates peony-like morphology in which the sulfide grows layered structures (Fig. S3b, ESI†). After the intercalation of PA, the peony-like structure was also maintained (Fig. 1a and b). Furthermore, the petal-like lamella of PA-MoS_2 was observed (Fig. 1c). The HRTEM image in Fig. 1d indicates the two interlayer distances of 0.62 and 0.98 nm, which both belong to the (002) phase of PA-MoS_2. The formation of 0.98 nm was due to the intercalation of PA enlarging the interlayer spacing. Besides, there exists a crystal defect-rich structure (Fig. 1d), in which the abundant crystal defects break the basal plane, enlarge the lattice spacing and reduce the energy barriers.[21–23] Besides, they also provide enough pathways on numerous edges to enhance the diffusion rate of zinc ions for the further improvement of the rate performance and long-term cycling stability of the PA-MoS_2 electrode. Energy dispersive spectroscopy-mapping profiles could verify the homogeneous distribution of S, Mo, O, C, and N throughout the PA-MoS_2 (Fig. 1e–h and Fig. S4a, b, ESI†).

In the XRD pattern of PA-MoS_2 (Fig. 2a), the interplanar spacing of the diffraction peak (002) was broadened to be 0.98 nm, which was corresponding to the description from the TEM image in

---

College of Materials Science and Metallurgy Engineering, Guizhou University, Guiyang 550025, P. R. China. E-mail: sjlu@gzu.edu.cn, yfzhang@gdut.edu.cn, hsfan@gzhu.edu.cn

† Electronic supplementary information (ESI) available. See DOI: **https://doi.org/10.1039/d2cc05888j**

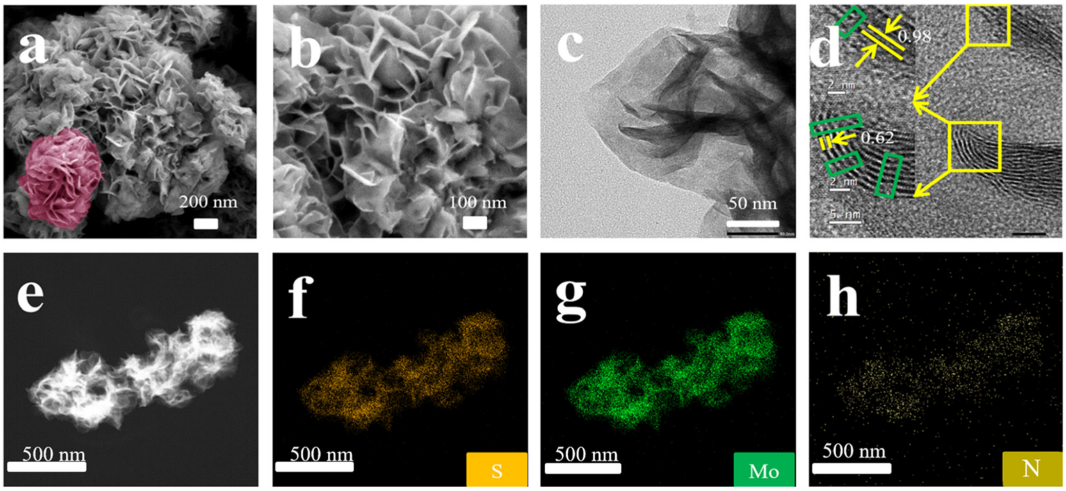

Fig. 1 (a and b) SEM images. (c and d) TEM images. (e and h) Elemental mappings of PA-MoS_2 (the green boxes present the lattice defects).

Fig. 1d. The chemical composition of PA-MoS_2 was investigated *via* XPS (Fig. 2b), which reveals the existence of the chemical composition of Mo, S, C, N, and O. Besides, the high-resolution Mo and S spectra are shown in Fig. 2c and d, respectively. In Fig. 2c, the two peaks of 231.5 and 228.35 were attributed to Mo^{4+} $3d_{3/2}$, and Mo^{6+} $3d_{5/2}$ of 2H phase MoS_2, respectively, indicating that there is no existence of $Mo^{4+}{}_{3d}$ of 1T phase MoS_2, which could illustrate the movement of the (002) crystal planes in Fig. 2a just only because of the expansion of the interlayer spacing rather than the formation of 1T phase MoS_2. Besides, the peaks located at 234.8 and 225.5 eV corresponded to Mo^{6+} $3d_{3/2}$ and S 2s, respectively. And the peak of Mo^{6+} $3d_{3/2}$ could be assigned to the surface oxidation. In Fig. 2d, the high-resolution S spectra could be split into S $2p_{1/2}$ (162.38 eV) and S $2p_{3/2}$ (161.28 eV).[24] Therefore, the pure 2H phase PA-MoS_2 was successfully attained.

In Fig. 3a, the initial three CV curves at 0.1 m V^{-1} s^{-1} were greatly repetitive and overlapped, which could prove the reversible Zn^{2+} de(intercalation) during the cycling process. Fig. 3b exhibits the rate properties of the PA-MoS_2 and MoS_2 at diverse current densities from 0.1 to 3 A g^{-1}. The specific capacities were reduced with the enhancement of the current densities, in which the electrode demonstrated the distinguished reversible capacity of 154.5, 119.4, 102.5, 91.3, 83.2, 76.0, and 63.9 mA h g^{-1} at 0.1, 0.5, 0.8, 1.2, 1.6, 2, and 3 A g^{-1}, respectively. Importantly, the discharge capacity was immediately increased to 146.7 mA h g^{-1} when the current density returned to 0.1 A g^{-1} from 3 A g^{-1}. However, the MoS_2 delivers a poor rate performance. It only delivers the specific capacity of 125.4, 83.4, 69.3, 62.9, 57.9, 52.9, and 44.3 at 0.1, 0.5, 0.8, 1.2, 1.6, 2, and 3 A g^{-1}. And when the current density is back to 0.1 A g^{-1}, the MoS_2 reveals a discharge capacity of 96.3 mA h g^{-1}. The PA-MoS_2 and MoS_2 both express the highly invertible insertion/extraction process of Zn^{2+} but the PA-MoS_2 exhibits a superior electrochemical property. Meanwhile, the galvanostatic charge/discharge (GDC) graph of rate performance was exhibited in Fig. 3c, in which the same charge/discharge plateaus could be seen. The PA-MoS_2 demonstrated prominent rate capability (Fig. 3d)[25–29] and outstanding cycling stability (Table S1, ESI†) in comparison with other reported molybdenum-based and other metal sulfides. PA-MoS_2 embraces the reversible capacity of 157.7 mA h g^{-1} at 0.1 A g^{-1} in the 80th cycle with a retention rate of about 100% (Fig. 3e). And the GDC curves at 0.1 A g^{-1} were demonstrated in Fig. 3f, in which the GDC curves reveal a greatly repetitive and overlapped ability. A similar voltage platform could be observed. The SEM images after cycling at 0.1 A g^{-1} were revealed. The particles next to the peony-like structure may be the conductive agent and binder agent. Though the structure was degraded after cycling, the peony-like structure and petal-like lamella of PA-MoS_2 could still be seen, which leads to prominent and stable cycling ability (Fig. S5a and b, ESI†). Besides, the long-term durable cycling stability is displayed in Fig. 3g, in which the material delivers an excellent specific property of 77.8 mA h g^{-1} at 1 A g^{-1}. And the galvanostatic charge-discharge curves are shown in Fig. S6 (ESI†), where there is only a slight attenuation. In particular, after 750 cycles, it not only maintains the coulombic efficiency of approximately 100% but also remains at the initial discharge capacity of 78.4%. In contrast, the MoS_2 only delivers 33.7 mA h g^{-1} at 1 A g^{-1} in the 750th cycle, manifesting that the intercalation of PA enhances

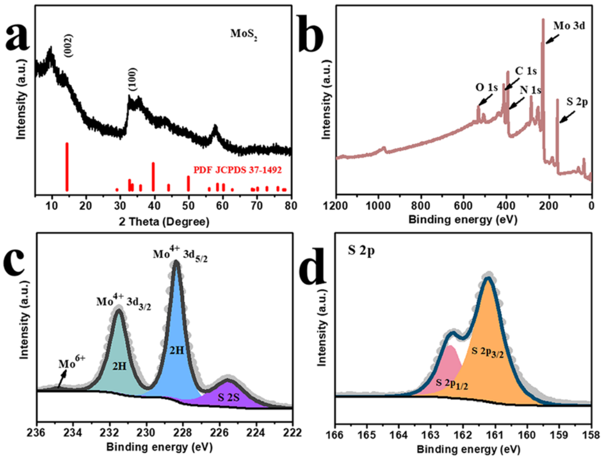

Fig. 2 (a) XRD pattern, and (b–d) XPS spectra of PA-MoS_2.

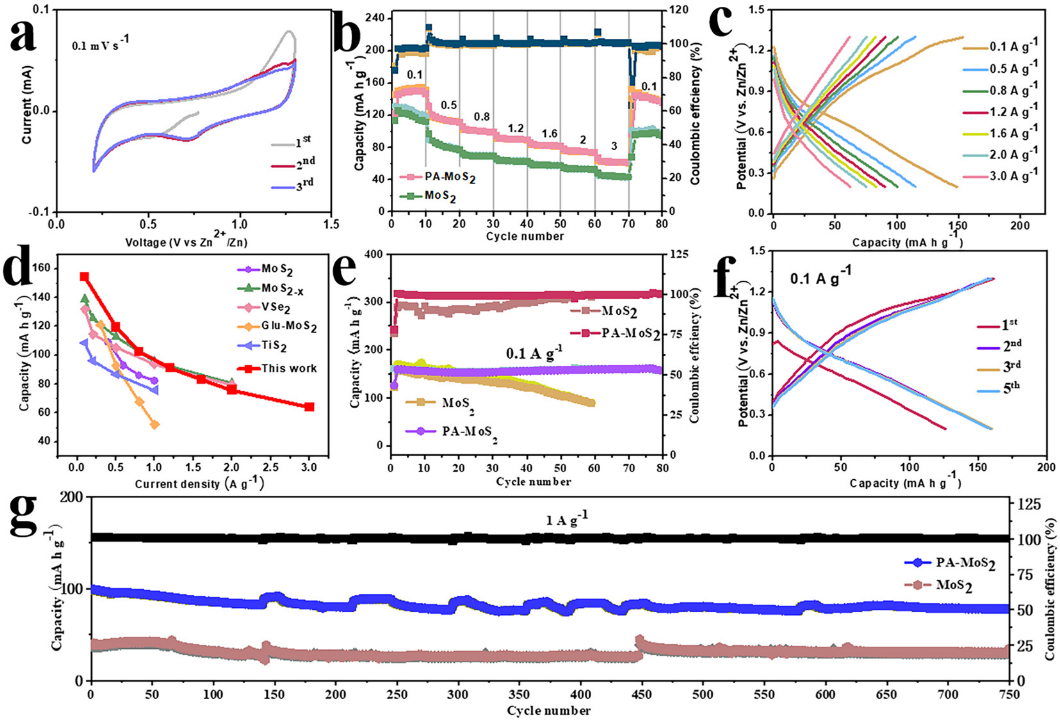

Fig. 3 (a) Initial three CV curves at 0.1 m V^{-1} s^{-1}. (b) Rate performance of PA-MoS$_2$ and MoS$_2$. (c) Galvanostatic charge–discharge profiles at different current densities of PA-MoS$_2$. (d) Comparison of the rate performance of PA-MoS$_2$ and other metal sulfides. (e) Cycling performance at 0.1 A g^{-1}. (f) Galvanostatic charge–discharge curves at 0.1 A g^{-1} of PA-MoS$_2$. (g) Long-term cycling stability at 1 A g^{1} of PA-MoS$_2$ and MoS$_2$.

the electrochemical performance of MoS$_2$ because the enlargement of the lattice spacing has a good effect on the reversible capacity.[25] Meanwhile, the defect-rich structure can effectively provide vast ion transport paths to enhance the ion diffusion rate.[26]

To further explore the kinetics of the as-prepared material, EIS and the galvanostatic intermittent titration technique (GITT) was tested. The Nyquist diagram indicates a semicircular curve associated with charge transfer between the electrolyte and the electrode at the high-frequency area and a diagonal line associated with ion diffusion at low frequency. The EIS pattern reveals the inherent resistance (R_s) and charge-transfer resistance (R_{ct}) of PA-MoS$_2$ at the initial cycle and after 10 cycle states (Fig. S7, ESI†). At the initial cycle, the electrode shows the low R_s of 0.92 Ω and R_{ct} of 115.8 Ω. After 10 cycles, both the inherent and charge transfer resistance was decreased (R_t = 0.84 Ω, R_{ct} = 42.26 Ω).

The diffusion coefficient zinc-ion diffusion of PA-MoS$_2$ (D_{Zn}) was calculated *via* the GITT method as the following equation:[30,31]

$$D_{\mathrm{Zn}} = \frac{4}{\pi\tau}\left(\frac{R_s}{3}\right)^2\left(\frac{\Delta E_s}{\Delta E_t}\right)^2 \tag{1}$$

in which the τ, R_s, ΔE_s, and ΔE_t serve as the relaxation time of the current pulse, the radius of the material particles, the voltage change in the charge pulse process, and the voltage change produced by galvanostatic dis(charge), respectively. The GITT curves of PA-MoS$_2$ at 0.1 A g^{-1} in the second cycle were exposed in Fig. 4a and b. After calculation, the D_{Zn} value of PA-MoS$_2$ stays in the magnitude range of 10$^{-13.4}$ to 10$^{-14.8}$ cm^2 s^{-1} and 10$^{-13.4}$ to 10$^{-15.2}$ cm^2 s^{-1} over an entire discharge and charge process, respectively (Fig. S8, ESI†).

The CV test under various scan rates from 0.1 to 1 m V^{-1} s^{-1} was carried out to further explain the kinetics of the as-prepared material (Fig. 4c). With the enhancement of the scan rate, the CV curves show a similar shape but the mild movement of the anodic and cathodic peaks due to the electrode polarization, and the oxidation and reduction peaks are positioned at around 1.01 and 0.71 V, respectively. Meanwhile, its charge–discharge behavior was measured *via* the equation of scan rate (v) and peak current (i): $i = av^b$, in which the b value ranges from 0.5 to 1.0. When the b value is 0.5 and 1.0, the electrochemical process is controlled by faradaic intercalation/deintercalation and the absolute surface capacitance, respectively. As shown in Fig. S9 (ESI†), the b value of the anodic and cathodic peaks was estimated to be 0.74 (peak 1) and 0.71 (peak 2), respectively. In addition, the peak current can also be composed of capacitive contribution (k_1v) and diffusion contribution ($k_2v^{1/2}$), and the equation is as follows:[32]

$$i = k_1v + k_2v^{1/2} \tag{2}$$

Furthermore, the equation could be transformed to:

$$i/v^{1/2} = k_1v^{1/2} + k_2 \tag{3}$$

Based on the CV curves and shaded region in Fig. 4d, it could be seen that *ca.* 69.9% of the whole capacity belongs to the capacitance at 1 m V^{-1} s^{-1} of scan rate. The proportions of capacitive influence and diffusion contribution were revealed in Fig. 4e during the dis(charge) process at various scan rates from 0.1 to 1.0 m V^{-1} s^{-1}. The capacitive contribution was 69.9, 66.4, 62.1, 57.4, 49.1, and 40.3% at the scan rates

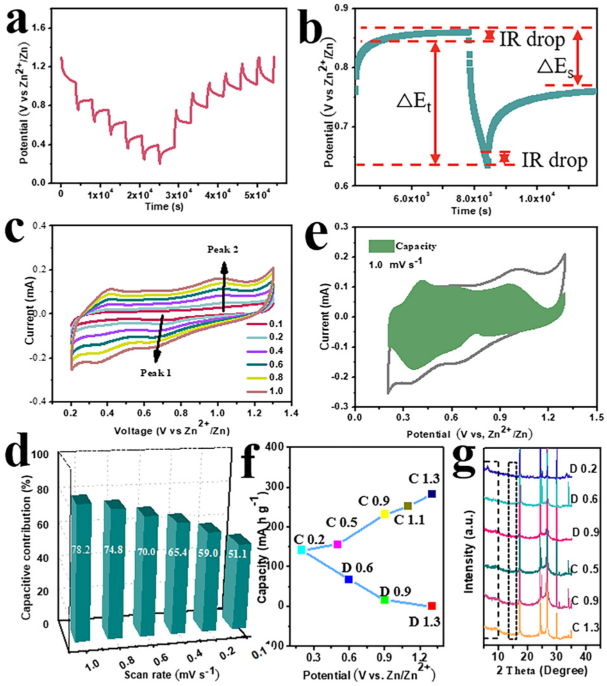

Fig. 4 (a and b) GITT curves at 0.1 A g^{-1}. (c) CV curves at different scan rates from 0.1 to 1.0 m V^{-1} s^{-1}. (d) Contribution ratio of the capacitance and diffusion at 0.6 m V^{-1} s^{-1}. (e) Contribution ratio of the capacitance and diffusion. (f) The galvanostatic charge–discharge curves of PA-MoS_2 in the 2nd cycle at 0.1 A g^{-1}. (g) Ex-situ XRD images of selected states.

of 1.0, 0.8, 0.6, 0.4, 0.2, and 0.1 m V^{-1} s^{-1}, respectively. Fig. 4f shows the dis(charge) states at different voltages in the 2nd cycle at a current density of 0.1 A g^{-1}. As shown in Fig. 4g, this diffraction peak from 15 to 35 Å belongs to electrolytes and carbon cloth. Besides, during the discharge process, the diffraction peak of *ca.* 9.1 Å was shifted negatively with the insertion of zinc ions. When the PA-MoS_2 was discharged from 0.2 V, the interlayer distance of the diffraction peak was shifted to 0.65 nm. Furthermore, as the charge voltage increases during the charging process, the diffraction peak was shifted positively.

In this paper, layer structured PA-MoS_2 with polyaniline intercalation and crystal defects was successfully prepared, which exhibits a high specific capacity of 157.7 mA h g^{-1} at 0.1 A g^{-1} after 80 cycles for the cathode of AZIBs. The reversible capacity of PA-MoS_2 was 77.8 mA h g^{-1} at a high current density of 1 A g^{-1}, and the retention rate was near 100% after 750 cycles. The enlarged lattice spacing and the defect-rich structure can effectively provide vast ion transport paths to enhance the ion diffusion rate. Meanwhile, the intercalated PA between the layers serves as a "pillaring" to support the structural stability during the charge–discharge process, all of which is conducive to excellent zinc ion storage properties.

This work was supported by National Natural Science Foundation of China (52101243), Natural Science Foundation of Guangdong Province (2020A1515010886) and the Science and Technology Planning Project of Guangzhou (202102010373).

Conflicts of interest

The authors declare that they have no conflict of interest.

References

1 D. Zhao, Z. Zhang, J. Ren, Y. Xu, X. Xu, J. Zhou, F. Gao, H. Tang, S. Liu, Z. Wang, D. Wang, Y. Wu, X. Liu and Y. Zhang, *Chem. Eng. J.*, 2023, **451**, 138882.
2 X. Liu, Z. Liu, W. Yang, M. Wang, B. Qin, Y. Zhang, Z. Liu and H. Fan, *Mater. Today Chem.*, 2022, **26**, 101002.
3 Q. Deng, M. Wang, X. Liu, H. Fan, Y. Zhang and H. Yang, *J. Colloid Interface Sci.*, 2022, **626**, 700–709.
4 M. Wang, X. Liu, B. Qin, Z. Li, Y. Zhang, W. Yang and H. Fan, *Chem. Eng. J.*, 2023, **451**, 138508.
5 X. L. Liu, F. Xu, Z. Y. Li, Z. T. Liu, W. Yang, Y. F. Zhang, H. S. Fan and H. Y. Yang, *Coord. Chem. Rev.*, 2022, **464**, 214544.
6 Z. Li, R. Sun, Z. Qin, X. Liu, C. Wang, H. Fan, Y. Zhang and S. Lu, *Mater. Chem. Front.*, 2021, **5**, 4401–4423.
7 C. Lin, X. Yang, P. Xiong, H. Lin, L. He, Q. Yao, M. Wei, Q. Qian, Q. Chen and L. Zeng, *Adv. Sci.*, 2022, **21**, 2201433.
8 F. Gao, B. Mei, X. Xu, J. Ren, D. Zhao, Z. Zhang, Z. Wang, Y. Wu, X. Liu and Y. Zhang, *Chem. Eng. J.*, 2022, **448**, 137742.
9 R. Sun, Z. Qin, X. Liu, C. Wang, S. Lu, Y. Zhang and H. Fan, *ACS Sustainable Chem. Eng.*, 2021, **9**, 11769–11777.
10 S. Li, J. Pan, F. Li, L. Zhang, D. Chai, Z. Zhang and J. Xin, *Dalton Trans.*, 2020, **49**, 10203–10211.
11 C. Zhu, G. Fang, J. Zhou, J. Guo, Z. Wang, C. Wang, J. Li, Y. Tang and S. Liang, *Mater. Chem. A*, 2018, **6**, 9677–9683.
12 H. Luo, B. Wang, F. Wang, J. Yang, F. Wu, Y. Ning, Y. Zhou, D. Wang, H. Liu and S. Dou, *ACS Nano*, 2020, **14**, 7328–7337.
13 Y. Ding, Y. Peng, S. Chen, X. Zhang, Z. Li, L. Zhu, L.-E. Mo and L. Hu, *ACS Appl. Mater. Interfaces*, 2019, **11**, 44109–44117.
14 X. Peng, H. Guo, W. Ren, Z. Su and C. Zhao, *Chem. Commun.*, 2022, **56**, 11803–11806.
15 X. Yuan and X. Li, *ChemistrySelect*, 2020, **5**, 13748–13753.
16 P. He, M. Yan, G. Zhang, R. Sun, L. Chen, Q. An and L. Mai, *Adv. Energy Mater.*, 2017, **7**, 1601920.
17 J. Liu, P. Xu, J. Liang, H. Liu, W. Peng, Y. Li, F. Zhang and X. Fan, *Chem. Eng. J.*, 2020, **389**, 124405.
18 H. Li, Q. Yang, F. Mo, G. Liang, Z. Liu, Z. Tang, L. Ma, J. Liu, Z. Shi and C. Zhi, *Energy Storage Mater.*, 2019, **19**, 94–101.
19 H. Liu, J.-G. Wang, W. Hua, Z. You, Z. Hou, J. Yang, C. Wei and F. Kang, *Energy Storage Mater.*, 2021, **35**, 731–738.
20 S. Li, Y. Liu, X. Zhao, Q. Shen, W. Zhao, Q. Tan, N. Zhang, P. Li, L. Jiao and X. Qu, *Adv. Mater.*, 2021, **33**, 2007480.
21 S. Li, Y. Liu, X. Zhao, K. Cui, Q. Shen, P. Li, X. Qu and L. Jiao, *Angew. Chem., Int. Ed.*, 2021, **60**, 20286–20293.
22 M. O. Enikeeva, K. M. Kenges, O. V. Proskurina, D. P. Danilovich and V. V. Gusarov, *Russ. J. Appl. Chem.*, 2020, **93**, 540–548.
23 W. Xu, C. Sun, K. Zhao, X. Cheng, S. Rawal, Y. Xu and Y. Wang, *Energy Storage Mater.*, 2019, **16**, 527–534.
24 C. Cai, Z. Tao, Y. Zhu, Y. Tan, A. Wang, H. Zhou and Y. Yan, *Nanoscale Adv.*, 2021, **13**, 3780–3787.
25 Y. Yang, *Int. J. Electrochem. Sci.*, 2020, **15**, 6052–6059.
26 W. Xu, C. Sun, K. Zhao, X. Cheng, S. Rawal, Y. Xu and Y. Wang, *Energy Storage Mater.*, 2019, **16**, 527–534.
27 L. Wang, M. Jiang, F. Liu, Q. Huang, L. Liu, L. Fu and Y. Wu, *Energy Fuel*, 2020, **34**, 11590–11596.
28 Y. Q. Jin, H. Chen, L. Peng, Z. Chen, L. Cheng, J. Song, H. Zhang, J. Chen, F. Xie, Y. Jin, J. Shi and H. Meng, *Chem. Eng. J.*, 2021, **416**, 127704.
29 Z. Wu, C. Lu, Y. Wang, L. Zhang, L. Jiang, W. Tian, C. Cai, Q. Gu, Z. Sun and L. Hu, *Small*, 2020, **16**, 2000698.
30 Q. Deng, X. Liu, Z. Li, H. Fan, Y. Zhang and H. Yang, *J. Colloid Interface Sci.*, 2023, **633**, 480–488.
31 M. Jia, W. Zhang, X. Cai, X. Zhan, L. Hou, C. Yuan and Z. Guo, *J. Power Sources*, 2022, **543**, 231843.
32 X. Li, H. Liang, B. Qin, M. Wang, Y. Zhang and H. Fan, *J. Colloid Interface Sci.*, 2022, **625**, 41–49.